J. Fluid Mech. (2007), *vol.* 587, *pp.* 217–234.
doi:10.1017/S002211200700732X Printed in the United Kingdom

Viscous flow past a flexible fibre tethered at its centre point: vortex shedding

LUODING ZHU
Department of Mathematical Sciences, Indiana University-Purdue University Indianapolis
Indianapolis, Indiana, USA
lzhu@math.iupui.edu

(Received 7 April 2006 and in revised form 26 April 2007)

Motivated by a laboratory experiment reported in Alben, Shelley & Zhang (*Nature*, vol. 420, 2002, p. 479), we performed simulations of an elastic fibre anchored at its centre point and immersed in a flowing viscous incompressible fluid by the immersed boundary (IB) method. We focus on the influence of some dimensionless parameters on vortex shedding from the fibre for Re in the range [30, 800]. Three sets of simulations were designed to investigate the influence of Reynolds number Re, dimensionless fibre flexure modulus $\hat{K}_b$, and dimensionless fibre length $\hat{L}$ on vortex shedding. According to the simulation results, Re, $\hat{K}_b$, and $\hat{L}$ each has a significant influence on the structure of shed vortices. However, Re has little influence on the vortex shedding frequency. With the increase of dimensionless bending modulus, the dimensionless vortex shedding frequency (f_{vs}) and the critical Reynolds number (Re_c) decrease approximately as power-law functions. Both f_{vs} and Re_c increase approximately linearly as dimensionless fibre length increases.

1. Introduction

Vortex shedding from an object immersed in a flowing fluid is an important and interesting topic and has been extensively studied experimentally, analytically and computationally (Sarpkaya 1979; Griffin & Ramberg 1982; Bearman 1989; Parkinson 1989; Williamson & Govardhan 2004). Most of the work has focused on vortex shedding from a rigid body. For instance, vortex shedding from a circular cylinder (tube) was studied by Abarbane *et al.* (1991), Nitsche & Krasny (1994), and Wang & Zhou (2005); from a sphere by Lee (2000); and from an (inclined) flat plate by Sarpkaya (1975) and Krasny (1990). Zhu & Peskin (2002, 2003) studied numerically the vortex shedding from elastic flapping filaments interacting with a flowing viscous fluid, and Jung *et al.* (2006) studied experimentally the vortex shedding from a flexible flapping rubber loop in a flowing soap film. Here we report our simulation of vortex shedding from a flexible fibre with its centre point tethered (otherwise unrestricted) in a two-dimensional flowing viscous incompressible fluid by the immersed boundary (IB) method (Peskin 1977; Peskin & McQueen 1996; Peskin 2002; Zhu & Peskin 2002).

The direct motivation of our work is a laboratory experiment reported in Alben, Shelley & Zhang (2002, 2004) and Alben (2004). The experiment used a flowing soap film (thickness 1–3 μm) as a flow tunnel. A flexible glass fibre (diameter 34 μm) was introduced with its middle point anchored at the centre of the flow channel and constrained nowhere else. The Reynolds number ranged from 2000 to 40 000 in the experiment. Alben *et al.* (2002, 2004) investigated the drag reduction induced by self-similar bending and streamlining of the fibre. Very recently, Zhu & Peskin (2007) computed the averaged drag of an elastic fibre immersed in a two-dimensional flowing incompressible viscous fluid at intermediate Reynolds numbers. One of the results was that when the inflow speed was sufficiently high, the flow became unsteady. Vortex shedding from the fibre became evident, the fibre vibrated and the drag coefficient versus time (C_d–t) curve oscillated.

This work investigates the influence of some dimensionless flow parameters on the vortex shedding. The flowing soap film was modelled by a two-dimensional viscous incompressible laminar channel flow, and the flexible fibre was simulated by a one-dimensional linear elastic curve. The fibre was assumed to be totally immersed and neutrally buoyant in the flowing fluid. The mathematical formulation and numerical method are based on the FFT version of the IB method (Peskin & McQueen 1996; Peskin 2002; Zhu 2001). This work investigates the vortex shedding at lower Reynolds numbers (30–800), focusing on the influence of the Reynolds number (Re), dimensionless fibre flexure modulus ($\hat{K}_b$), and dimensionless fibre length ($\hat{L}$) on the vortex shedding.

2. Governing equations

Using standard notation ($\boldsymbol{u}$ for velocity, ρ for mass density, p for pressure, $\boldsymbol{x}$ for Eulerian spatial coordinates, t for time, and α for the Lagrangian coordinate which was chosen as the fibre arc-length at the initial configuration and was frozen throughout a simulation), the equations governing the motion of both the fluid and the fibre (neutrally buoyant) in dimensionless form are as follows (the IB formulation):

$$\frac{\mathrm{D}\boldsymbol{u}(\boldsymbol{x},t)}{\mathrm{D}t} + \nabla p(\boldsymbol{x},t) = \frac{1}{Re}\Delta\boldsymbol{u}(\boldsymbol{x},t) + \boldsymbol{f}(\boldsymbol{x},t) - Fr^{-1}\boldsymbol{u}(\boldsymbol{x},t) - \boldsymbol{g}, \tag{1}$$

$$\nabla\cdot\boldsymbol{u}(\boldsymbol{x},t) = 0, \tag{2}$$

$$\boldsymbol{f}(\boldsymbol{x},t) = \int \boldsymbol{F}(\alpha,t)\delta(\boldsymbol{x} - \boldsymbol{X}(\alpha,t))\,\mathrm{d}\alpha, \tag{3}$$

$$\boldsymbol{F}(\alpha,t) = -\frac{\partial e}{\partial \boldsymbol{X}} = -\frac{\partial(e_s + e_b)}{\partial \boldsymbol{X}}, \tag{4}$$

$$e_s = \frac{1}{2L}\hat{K}_s \int \left(\left|\frac{\partial \boldsymbol{X}(\alpha,t)}{\partial\alpha}\right| - 1\right)^2 \mathrm{d}\alpha, \tag{5}$$

$$e_b = \frac{1}{2L}\hat{K}_b \int \left|\frac{\partial^2 \boldsymbol{X}(\alpha,t)}{\partial\alpha^2}\right|^2 \mathrm{d}\alpha, \tag{6}$$

$$\frac{\partial \boldsymbol{X}}{\partial t}(\alpha,t) = \boldsymbol{U}(\alpha,t), \tag{7}$$

$$\boldsymbol{U}(\alpha,t) = \int \boldsymbol{u}(\boldsymbol{x},t)\delta(\boldsymbol{x} - \boldsymbol{X}(\alpha,t))\,\mathrm{d}\boldsymbol{x}. \tag{8}$$

Here $\mathrm{D}/\mathrm{D}t = \partial/\partial t + \boldsymbol{u}\cdot\partial/\partial\boldsymbol{x}$ is the material derivative, the vector $\boldsymbol{g} = (0, Fr^{-1})^T$ and Fr is the Froude number. Re is the Reynolds number, e is the fibre elastic potential energy density, and e_s and e_b are fibre elastic energy density associated with compression/stretching and bending, respectively. $\hat{K}_s$ is the dimensionless stretching/compression coefficient, $\hat{K}_b$ is the dimensionless flexure modulus, and L is the fibre total length. See table 2 below for definitions of these non-dimensional quantities and their values used in the simulations.

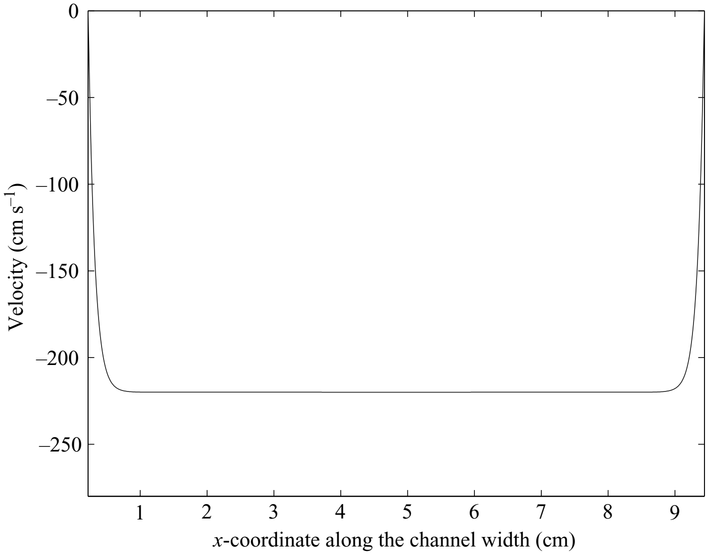

FIGURE 1. The initial velocity and inflow velocity profiles for inflow speed 220 cm s^{-1}. The x-axis represents the flow tunnel width direction. The y-axis is the second component (i.e. $v(x)$) of the velocity $\boldsymbol{u}(\boldsymbol{x}, 0)$. (Note v is a function of x only here and the first velocity component is zero.) The inflow velocity profile is flat on most of the channel except near the left and right boundaries; this is because of the air resistance. This profile is imposed as the initial condition and inlet/outlet boundary conditions for velocity.

Equations (1) and (2) are the incompressible viscous Navier–Stokes equations governing the motions of both the fluid and the fibre. The term $-Fr^{-1}\boldsymbol{u}$ is the air resistance, where the coefficient happens to be the reciprocal of the Froude number. (The dimensional air resistance coefficient, λ, was determined by the equation $\lambda|V_0| = \rho_0 g$. Here V_0 is the inflow speed, ρ_0 is the fluid mass density†, and g is the gravitational acceleration constant. If ρ_0, V_0 and L are chosen as reference quantities to non-dimensionalize the IB formulation, the air resistance term $-\lambda\boldsymbol{u}$ becomes $-g^*\boldsymbol{u}^*$, where the quantities with a $*$ denote their corresponding dimensionless equivalent. It turns out that $g^* = Fr^{-1}$ in our case.) Equation (7) updates the position and shape of the fibre. The fibre velocity $\boldsymbol{U}(\alpha, t)$ is interpolated by (8) from the velocity of the fluid. From the fibre configuration $\boldsymbol{X}(\alpha, t)$ the elastic potential energy density (e) is calculated via (5) and (6) and the Lagrangian force density $\boldsymbol{F}(\alpha, t)$ is computed through (4). The immersed boundary force $\boldsymbol{f}(\boldsymbol{x}, t)$ on the right-hand side of (1) is calculated using (3). Equations (1)–(8) constitute a nonlinear system of integral-differential equations which depicts the motions of the viscous fluid and the elastic fibre. The system is completed by imposing appropriated initial and boundary conditions. The initial velocity was the steady solution to the two-dimensional stationary channel flow under the action of gravity and air resistance in the absence of the fibre. See figure 1 for a typical initial velocity profile. The initial velocity profile was imposed on the inlet and outlet. The velocity was zero on the two side boundaries. The fibre middle point ($\boldsymbol{X}(s_c, t)$, where s_c is the Lagrangian coordinate for the middle point) was tethered at a fixed Eulerian point (x_0, y_0) by a virtual spring with the same stiffness as the inextensible fibre itself. It was found that $\boldsymbol{X}(s_c, t)$ was almost constant in all simulations.

† ρ is the mass density of the fluid–fibre system, ρ_0 is the mass density of the fluid. For a neutrally buoyant immersed structure as in our case, $\rho = \rho_0$.

Inflow speed (V_0)	50–300 $\mathrm{cm\,s^{-1}}$
Fluid kinematic viscosity (ν)	1–22 $\mathrm{cm^2\,s^{-1}}$
Fluid density (ρ_0)	$3 \times 10^{-4}\,\mathrm{g\,cm^{-2}}$
Fibre length (L)	1–5 cm
Fibre flexure modulus (K_b)	0.28–10^3 erg cm
Compression/stretching coeff (K_s)	$2.4 \times 10^6\,\mathrm{dyn\,cm^{-1}}$
Gravitational acceleration (g)	980 $\mathrm{cm\,s^{-2}}$
Width of the film (W)	2.0–9.0 cm
Height of the film (H)	18 cm

TABLE 1. Parameters used in the simulations.

Name	Definition	Range
Reynolds number (Re)	$V_0 L/\nu$	30–800
Froude number (Fr)	$V_0^2/(gL)$	3.09–91.84
Filament length ($\hat{L}$)	L/W	0.11–0.8
Dimensionless flexure modulus ($\hat{K}_b$)	$K_b/(\rho_0 V_0^2 L^3)$	2.89×10^{-4}–0.1037
Dimensionless stretching coeff ($\hat{K}_s$)	$K_s/(\rho_0 V_0^2 L)$	1.8×10^4–1.25×10^7

TABLE 2. Non-dimensional parameters used in the simulations. For the meanings of the symbols used in the definitions, see table 1.

3. Simulation results

The above nonlinear system of integral-differential equations was discretized on a non-staggered uniform fixed Eulerian grid. The backward Euler method was used for time derivatives and centre differencing was used for spatial derivatives (both gradient and divergence operators). The skew-symmetrical scheme was used for the convection term and the nonlinearity therein was removed by using the velocity at the previous time step. The immersed boundary force $\boldsymbol{f}$ was treated explicitly. The resultant linear algebraic system with constant coefficients was solved by the discrete fast Fourier transform (DFFT). The dimensionless time-step size was $\Delta t = 10^{-4}$. The spatial grid size was 256×512. See Peskin & McQueen (1996) and Zhu (2001) for the details of the discretization and how the algebraic system was solved by the DFFT.

The parameters (dimensional) used in our simulations are tabulated in table 1. Some parameters remained fixed throughout all the simulations reported here, and their values (as in table 1) will not be stated again for each simulation reported below. These include fluid density (ρ_0), gravitational acceleration constant (g), compression/stretching coefficient K_s, and height (H) of the computational domain.

In our simulations we used the values of all the dimensional parameters in the laboratory experiment except the fluid viscosity and the channel width. The viscosity is approximately 100 times greater than in the experiment which causes the Reynolds numbers in our simulations to be smaller by approximately two orders of magnitude. The channel width was fixed to be 9 cm in the experiment. In the simulations to investigate the influence of dimensionless fibre length, the channel width was varied from 9 cm to 2 cm. (Note that varying the fibre length causes changes not only in $\hat{L}$, but also in Re and $\hat{K}_b$. See table 2.) For all other simulations in this paper, the channel width was fixed to be 9 cm (the experimental value). The values of all the other dimensional and dimensionless parameters are within the experimental ranges.

In addition to the Reynolds (Re) and Froude numbers (Fr), our elastic-fibre–fluid problem (fibre neutrally buoyant in fluid) has the following other non-dimensional parameters: the dimensionless fibre flexure modulus ($\hat{K}_b$), the dimensionless fibre length ($\hat{L}$), and the dimensionless compression/stretching coefficient ($\hat{K}_s$). See table 2 for their definitions and values used in our simulations. In general it is expected that the vortex shedding and drag coefficient are outcomes of the interplay of these dimensionless quantities.

The fibre physical compression/stretching coefficient K_s was chosen such that the fibre was almost inextensible in all simulations: the relative increase and decrease in fibre length was less than 0.25 %. Even though $\hat{K}_s$ varied with V_0 and L, we assumed that the influence of $\hat{K}_s$ on the fluid–fibre problem was not important because it was very large in each case. The fibre mass density has been found to play no important role in the fibre drag coefficient (Zhu & Peskin 2007). Therefore the fibre was assumed to be neutrally buoyant in the fluid. Also, no significant influence of the Froude number Fr on the vortex shedding and fibre drag was expected. Therefore, the influence of $\hat{K}_s$ and Fr on vortex shedding will not be discussed, and only that of Reynolds number, dimensionless flexure modulus and dimensionless fibre length will be addressed explicitly.

To isolate the effect of Reynolds number, a series of simulations with varying fluid kinematic viscosity was performed. Note that only the Reynolds number varied from simulation to simulation throughout the series. All the other dimensionless parameters were constant. An analogous series of simulations was performed to single out the influence of the dimensionless flexure modulus. In this series only the dimensional flexure modulus (K_s) varied. Therefore only $\hat{K}_b$ varied throughout this series of simulations. The third series of simulations was run to show the influence of the dimensionless fibre length, with only the channel width W being varied in this series.

The instantaneous drag (D) the fibre experiences is computed the same way as in Zhu & Peskin (2007). The drag coefficient is defined as $C_d = D/(\frac{1}{2}\rho_0 {V_0}^2 L)$. A time-averaged drag coefficient $\bar{C}_d$ is defined as $\bar{C}_d = \bar{D}/(\frac{1}{2}\rho_0 {V_0}^2 L)$. Here $\bar{D}$ is the time-averaged drag which is computed over N equally spaced instants between times T_{qs} and T_e. Here T_{qs} is some time after the initial transition dies out and the fibre reaches a small-amplitude oscillation state ('quasi-steady' state for short). $T_{qs} = 10$ for this work. The simulation terminal time T_e and the time spacing between two neighbouring instantaneous drag computations T_s are chosen arbitrarily. In this work $T_s = 0.05$, and $T_e = 24$–30.

The remainder of this section is structured as follows. First the influence of Re on vortex shedding and drag coefficient is discussed. Then follows the influence of $\hat{K}_b$. The third part addresses the influence of the dimensionless fibre length.

3.1. *Influence of Reynolds number*

To investigate the influence of Re, a series of simulations with different kinematic viscosity ν was performed. The fluid kinematic viscosity ν ranged from 1 to 22 $\text{cm}^2\,\text{s}^{-1}$. The corresponding Re ranged from 30 to 800. The other parameters used in this series of simulations were as follows: $L = 3.3\,\text{cm}$, $V_0 = 200\,\text{cm}\,\text{s}^{-1}$, $K_b = 2.8\,\text{erg}\,\text{cm}$. The values of dimensionless parameters were: $\hat{K}_b = 6.5 \times 10^{-3}$, $\hat{L} = 0.37$, $Fr = 12.37$, $\hat{K}_s = 6.1 \times 10^4$. Four typical simulation results are shown in figure 2. In this figure, the top panels plot the instantaneous positions of fluid markers (used to visualize the fluid motion) at time $T = 24$ (dimensionless). The markers were released on the inlet boundary periodically. They were massless and moved with the fluid. Their velocity was interpolated from that of the fluid exactly as the fibre velocity was computed. The lower panels plot the corresponding vorticity contours (for visualization of the vortical field) at the same time instant. These four typical simulations show the influence of

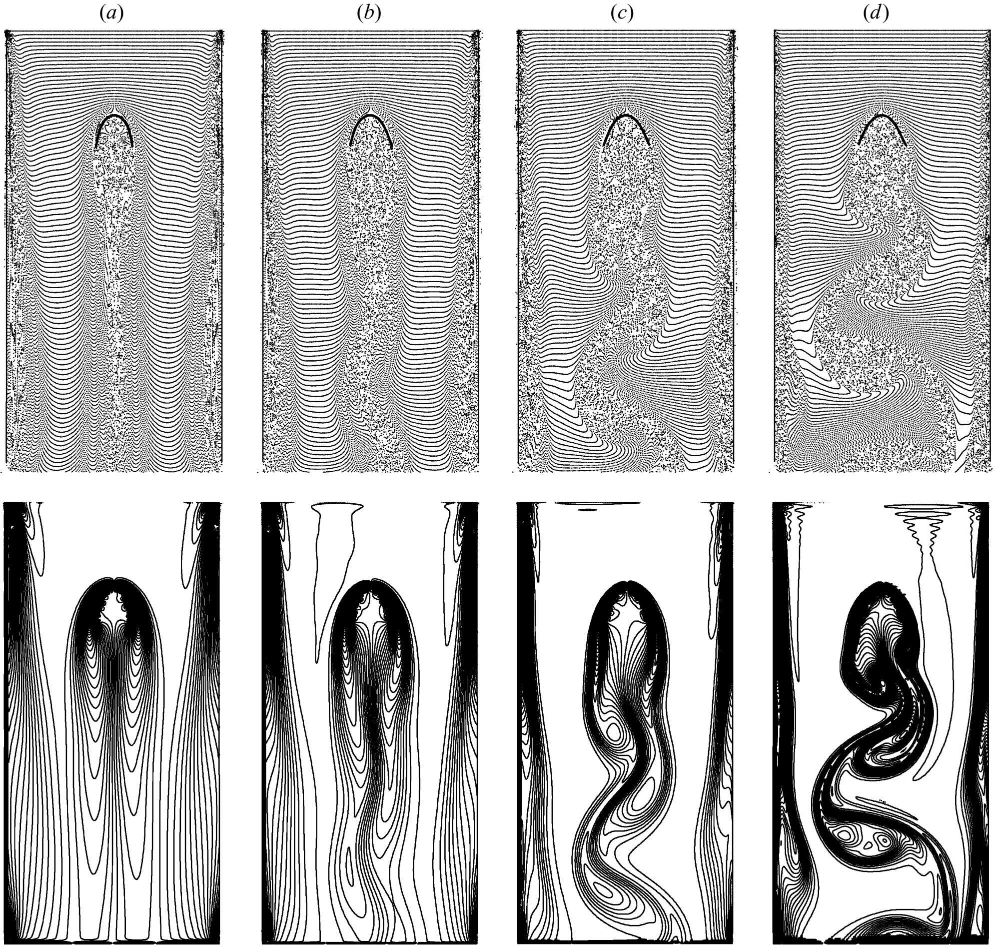

FIGURE 2. Visualization of the flow and vortical field at four different Reynolds numbers at dimensionless time 24. The upper panels are the instantaneous positions of fluid markers at four different instants and the lower panels are the vorticity contours at corresponding time. The Reynolds number is (*a*) 82.5, (*b*) 165, (*c*) 330, (*d*) 660.

the Reynolds number on vortex shedding. Vortex shedding is not observed when the Reynolds number $Re \leqslant 155$. When the Reynolds number is around 165, vortex shedding starts to appear. With the increase of Re the vortex shedding becomes more apparent and intensive. The wake zone behind the fibre widens. The vortices shed become nearly perpendicular to the mainstream flow from being nearly aligned with the flow. (A shed vortex can be roughly approximated as an ellipse. The ellipse's long axis is used to determine whether the vortex is perpendicular to or aligned with the mainstream direction.)

Figure 3 demonstrates the influence of Re on the motion of the fibre and the drag coefficient C_d for the above four typical simulations. The upper panels plot C_d versus time; the lower panels plot the fibre position and shape for the corresponding case. Dotted lines are used for $t \leqslant T_{qs}$ and solid lines for $t \geqslant T_{qs}$. The thickness of the solid dark line indicates the range of oscillation. The fibre vibrates within this range after T_{qs}. From figure 3 we can see that with the increase of Reynolds number,

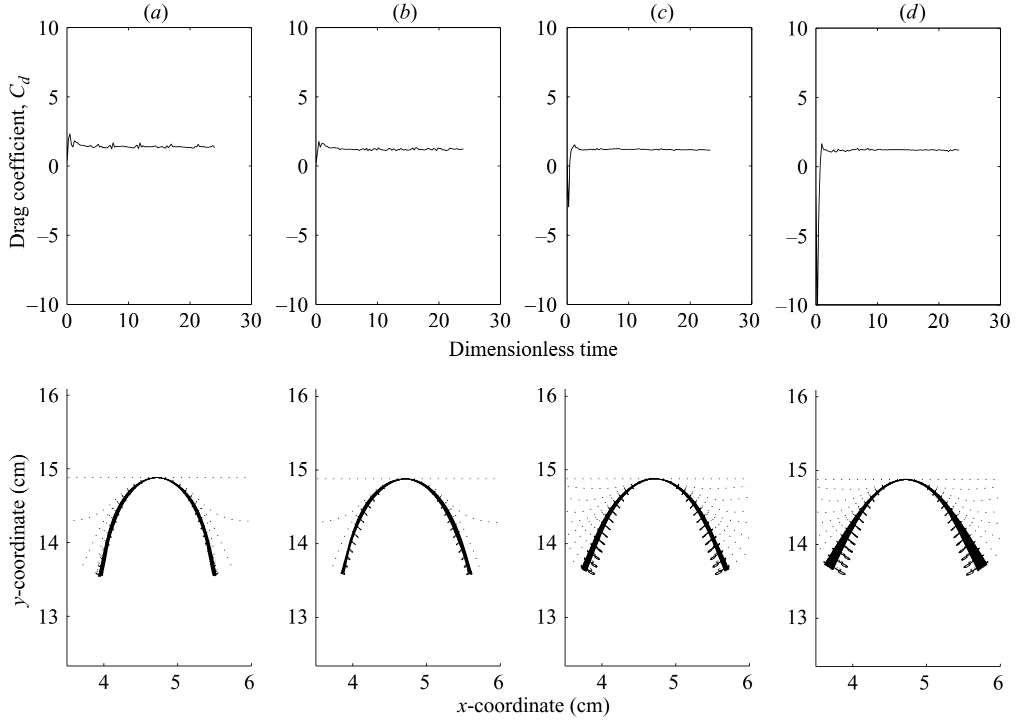

FIGURE 3. The drag coefficient versus dimensionless time and position of the fibre at four different Reynolds numbers. The upper panels plot the drag coefficient as a function of time and the lower panels plot the corresponding position of the fibre. The dotted and solid lines are the fibre positions before and after it reaches the 'quasi-steady' state, respectively. The thickness of the solid lines (many lines overlap) represents the fibre oscillation range. The Reynolds number Re is (a) 82.5, (b) 165, (c) 330, (d) 660.

the opening of the parabola (fibre positions) widens and the fibre oscillation range increases (the dark line thickens). However, the drag coefficient of the fibre seems to be quite insensitive to the Reynolds number within the range 200 to 800. The drag coefficient-versus-time curves (C_d–t curve) look quite similar to each other (notice that the curve for $Re = 82.5$ is slightly above the other three). One might expect that the C_d–t curve would becomes more oscillatory with the increase of Reynolds number as a consequence of intensified fibre vibration (probably induced by enhanced vortex shedding). But according to our simulations, this is not the case. The drag coefficient C_d versus Re is given in figure 4 for Reynolds number range [30, 800]. It is seen that C_d is roughly constant for Re between 200 and 800, but when Re gets smaller than approximately 200, the drag coefficient begins to increase, first slightly and then rapidly. It seems that the increase of shape drag is offset well by the decrease of friction drag as Re increases in the range (200, 800). When Re become sufficiently small, the increase of friction drag starts to dominate and thus causes a significant increase in the drag coefficient.

A critical Reynolds number Re_c for vortex shedding is defined as the value at which the steady wake becomes unstable (sustained wake oscillation begins) after the initial transition period. It was found that Re_c varies with the dimensionless fibre modulus and length. It is 82 ± 5 by the method of bisection for the values of $\hat{K}_b$ and $\hat{L}$ used for this set of simulations. The vortex shedding frequency is not sensitive to Re in the

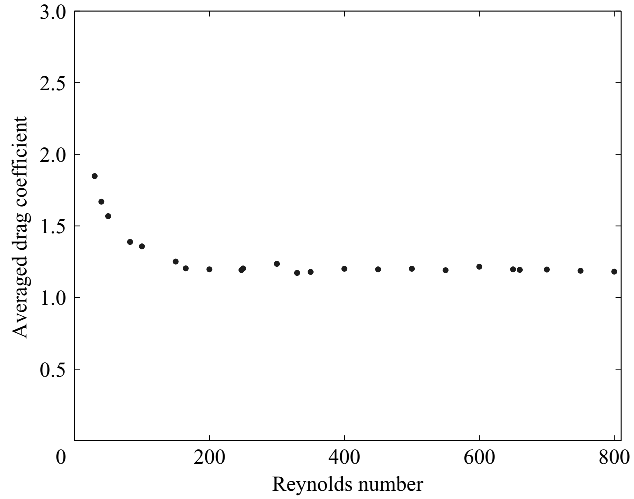

FIGURE 4. Averaged drag coefficient $\bar{C}_d$ versus Reynolds number Re. The drag coefficient varies very slowly with Reynolds number ($\bar{C}_d$ is nearly a constant) for Re between 200 and 800, and increases rapidly when Re gets smaller.

range (160, 800) where vortex shedding is obvious. It is roughly a constant equal to 75. Non-dimensionalized by V_0/L, the dimensionless vortex shedding frequency f_{vs} is approximately 1.2.

Based on the sequence of simulations with Re range [30, 800], we may conclude that while the Reynolds number has significant influence on the structure of shed vortices, it has little influence on the vortex shedding frequency and the averaged drag coefficient ($\bar{C}_d$) for Re in (200, 800).

3.2. *Influence of dimensionless flexure modulus*

A series of simulations with varying flexure modulus ($\hat{K}_b$) was performed to explore its influence on the vortex shedding and drag coefficient. All other parameters were kept the same. The value of $\hat{K}_b$ varied from 0.1037 to 2.89×10^{-4}. The other dimensionless parameters were: $Re = 247.5$, $\hat{L} = 0.37$, $Fr = 27.83$, $\hat{K}_s = 2.69 \times 10^4$. The inflow speed was $V_0 = 300\,\mathrm{cm\,s^{-1}}$, the fibre was 3.3 cm long. See figure 5 for four typical simulation results with different flexure modulus. From this figure we see that the flexure modulus has a significant influence on the structure of shed vortices. As $\hat{K}_b$ decreases, the fibre becomes more flexible. It bends and is streamlined more easily. The wake behind the fibre narrows and the vortices shed look quite different. As $\hat{K}_b$ decreases, the shed vortices are approximately aligned with the mainstream flow at first, then become nearly perpendicular to the flow, and finally return to the state of being aligned with the flow. Figure 6 plots the drag coefficient versus time and the position of the fibre. As the flexure modulus decreases between 0.1037 and 1.44×10^{-3} fibre vibration becomes more violent. Consequently the C_d–t curve becomes more oscillatory. When the flexure modulus is further decreased, the fibre becomes more aligned with the flow and less fibre oscillation is seen. Consequently the C_d–t curve is less oscillatory. This may be explained as follows. To oscillate in this situation (the majority of the fibre is almost parallel to the mainstream flow), the fibre has to displace more fluid with larger momentum in the vertical direction (y-component of momentum). This restricts the motion of the fibre. Therefore, the fibre vibrates in a narrower range and the C_d–t curve is less oscillatory. Note that the drag coefficient as a function of

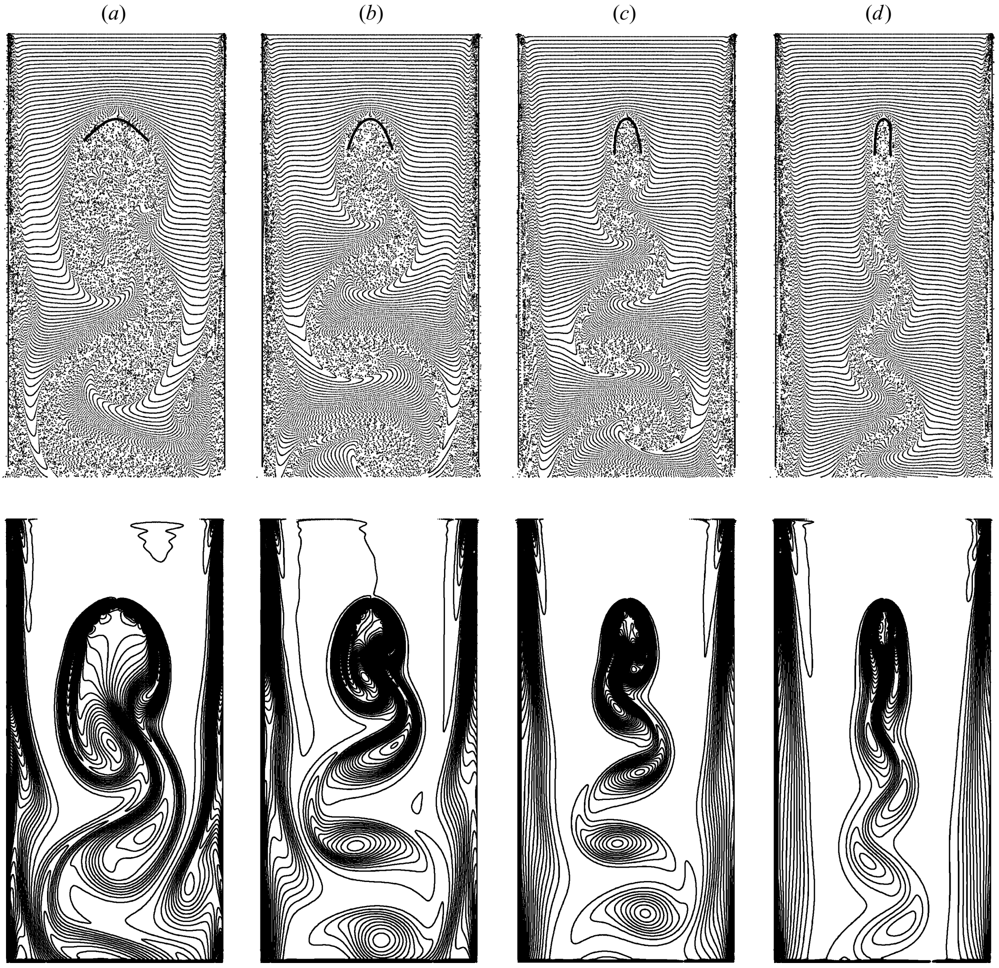

FIGURE 5. Visualization of the flow and vortical field at dimensionless time 30. The upper panels are the instantaneous positions of fluid markers and the lower panels are the vorticity contours. The value of $\hat{K}_b$ is (*a*) 2.89×10^{-2}, (*b*) 7.21×10^{-3}, (*c*) 1.44×10^{-3}, and (*d*) 2.89×10^{-4}.

time monotonically decreases as the flexure modulus decreases as shown in the top panels of figure 6 (see Zhu & Peskin 2007 for a detailed C_d–$\hat{K}_b$ plot). This is probably because the shape drag dominates the total drag and apparently it becomes smaller the fibre gets more and more aligned with the mainstream flow, due to the decrease in flexure modulus.

Figure 7(*a*) plots the dimensionless vortex shedding frequency f_{vs} versus dimensionless bending modulus $\hat{K}_b$; panel (*b*) is a log-log plot. The data on the log-log scale is best fitted by the line $y = -0.14x - 0.77$. This indicates that f_{vs} decreases as a power-law function of $\hat{K}_b$ in the range $(10^{-4}, 0.1)$, i.e. $f_{vs} \sim \hat{K}_b^{-0.14}$. This may be qualitatively explained as follows: the smaller the $\hat{K}_b$, the more flexible the fibre, as a consequence the fibre is more aligned with the mainstream flow, and thus the vortices formed and attached to the fibre is washed away more easily by the mainstream flow.

Figure 8 plots on a log-log scale the critical Reynolds number for vortex shedding Re_c (defined as in § 1) as a function of dimensionless bending modulus $\hat{K}_b$. The data

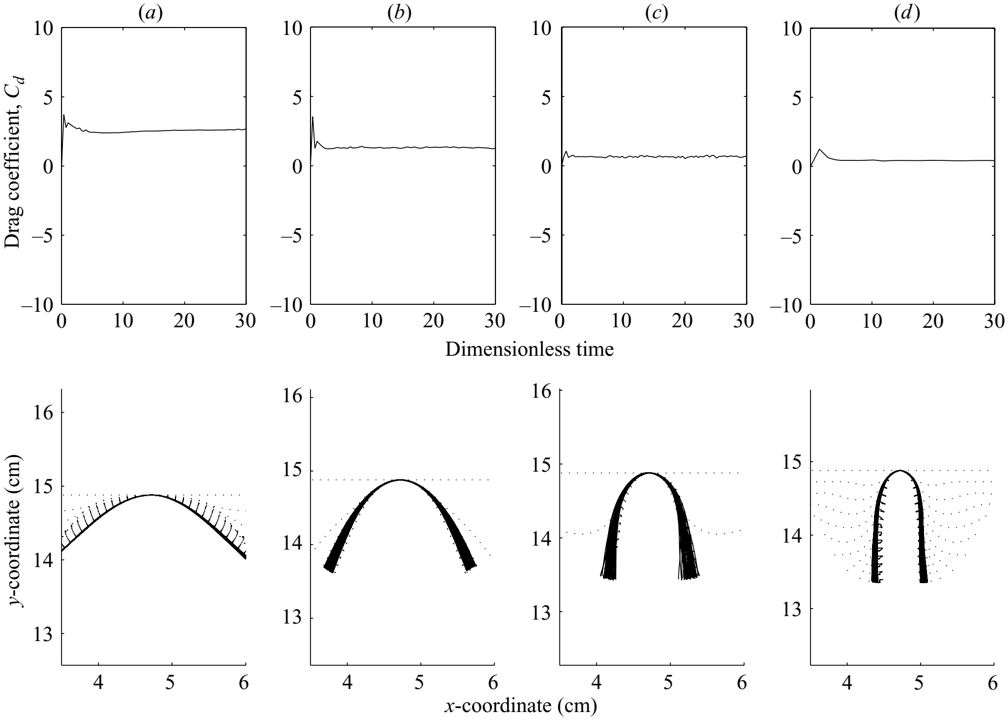

FIGURE 6. The drag coefficient and position of the fibre at four different values of the dimensionless bending rigidity $\hat{K}_b$. The upper panels plot the drag coefficient as a function of time and the lower panels plot the corresponding position of the fibre. The dotted and solid lines are the fibre positions before and after it reaches the 'quasi-steady' state, respectively. The thickness of the solid lines (many lines overlap) represents the fibre oscillation range. The value of $\hat{K}_b$ is (*a*) 2.89×10^{-2}, (*b*) 7.21×10^{-3}, (*c*) 1.44×10^{-3}, (*d*) and 2.89×10^{-4}.

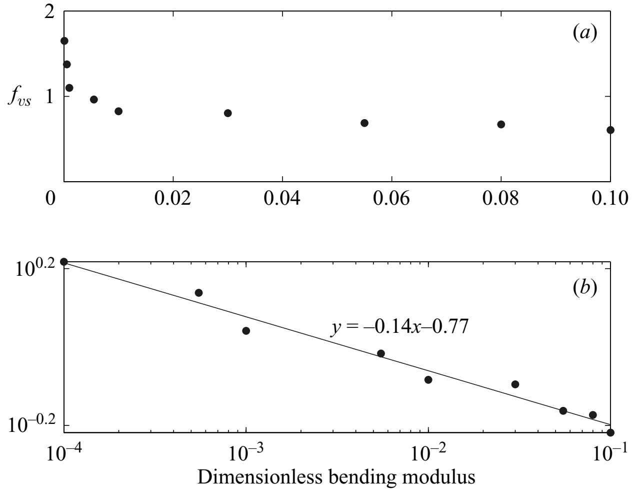

FIGURE 7. Dimensionless vortex shedding frequency f_{vs} versus dimensionless bending modulus $\hat{K}_b$. (*a*) f_{vs} as a function of $\hat{K}_b$; (*b*) a log-log plot of the data. The line $y = -0.14x - 0.77$ fits the data best in the least squares sense. This shows that f_{vs} decreases approximately as $\hat{K}_b^{-0.14}$ which is valid for $\hat{K}_b$ in $(10^{-4}, 10^{-1})$.

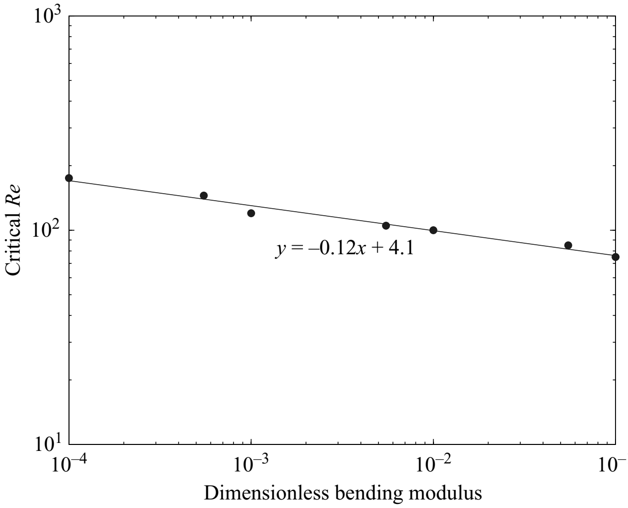

FIGURE 8. A log-log plot of critical Reynolds number Re_c for vortex shedding versus dimensionless bending modulus $\hat{K}_b$. The critical Reynolds number decreases as the dimensionless bending modulus increases. The best-fitting line by the least squares is $y = -0.11x + 4.1$. The data of Re_c contain an error of ±5.

are best fitted by the line $y = -0.12x + 4.1$ in the least squares sense which indicates that the Re_c decreases approximately in a power law with $\hat{K}_b$ in the range $(10^{-4}, 0.1)$ i.e. $Re_c \sim \hat{K}_b^{-0.12}$. Re_c is determined by the bisection method and has an error of ±5.

At first glance the above two results seem to be contradictory. One would expect that an increase of vortex shedding frequency as $\hat{K}_b$ becomes smaller would indicate vortex shedding becomes easier as $\hat{K}_b$ decreases, and thus the critical Reynolds number should decrease as $\hat{K}_b$ decreases. However this is not true according to our simulations. The reason is as follows: Re_c is defined as the minimum Reynolds number that causes sustained oscillation of the wake. As $\hat{K}_b$ decreases the fibre becomes more aligned with the mainstream flow and represents a smaller and smoother obstacle to the flow. Therefore the wake becomes narrower and self-sustained oscillation becomes more difficult (the narrower wake is constrained on both sides by widened mainstream flow with greater momentum along the y-direction).

Based on the sequence of simulations with $\hat{K}_b$ in $[2.89 \times 10^{-4}, 0.1037]$, it may be concluded that the fibre dimensionless flexure modulus has a significant influence on the vortex shedding, the fibre vibration, and the C_d–t curve. When $\hat{K}_b$ increases in the above range, both f_{vs} and Re_c decrease approximately as power laws in $\hat{K}_b$.

3.3. *Influence of dimensionless fibre length*

To study the influence of the dimensionless fibre length on vortex shedding, a group of simulations with different channel width W were performed. W ranged from 2 to 9 cm. All the other dimensional parameters were kept the same for all simulations in the group: $L = 1.6\,\text{cm}$, $V_0 = 200\,\text{cm s}^{-1}$, $\nu = 2.1333\,\text{cm}^2\,\text{s}^{-1}$, $K_b = 0.25\,\text{erg cm}$. The four typical cases are depicted in figure 9. The dimensionless fibre length $\hat{L}$ for these four cases was 0.1778, 0.4, 0.6 and 0.8. The corresponding Reynolds number was 150, the dimensionless flexure modulus was 0.005086, Fr was 25.51, and $\hat{K}_s$ was 1.25×10^7.

Figure 9 demonstrates that the $\hat{L}$ has a significant influence on vortex shedding. As $\hat{L}$ increases in (0.17, 0.8), the number of shed vortices increases (i.e. the shedding frequency increases). The shed vortices are detached from each other initially, but

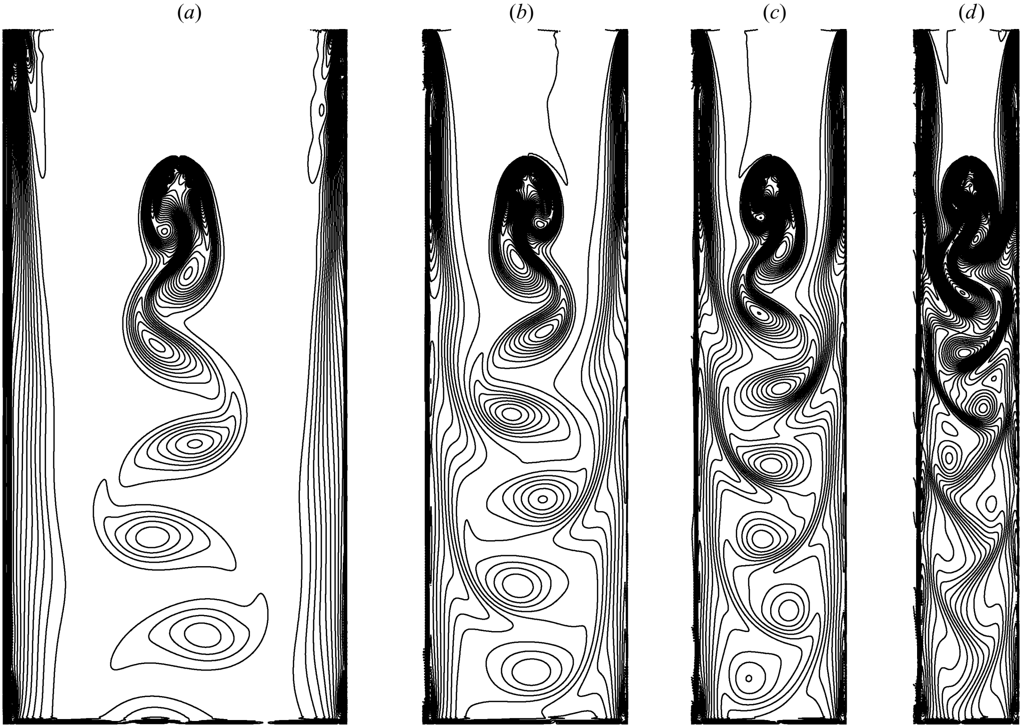

FIGURE 9. Visualization of vortical field: the vorticity contours for four different dimensionless fibre length $\hat{L}$ at dimensionless time 30, (*a*) 0.1778, (*b*) 0.4, (*c*) 0.6, (*d*) 0.8.

become somewhat attached to each other as $\hat{L}$ increases. The wake zone becomes narrower and the shed vortices directly interact with the boundary layers as they are carried away downstream.

Figure 10 plots the drag coefficient as a function of time and the position of the fibre at the 'quasi-steady' state. With the increase of $\hat{L}$, the opening of the fibre contracts gradually and it becomes more aligned with the flow (although $\hat{K}_b$ was fixed). The height of the C_d–t curve increases slightly with the increase of $\hat{L}$. The degree of oscillation in the C_d–t curve is roughly the same. Figure 11 plots the averaged drag coefficient $\bar{C}_d$ versus $\hat{L}$. It is interesting to notice that the averaged drag coefficient (after T_{qs}) is an increasing function of the dimensionless fibre length. One may expect that as W decreases (i.e. $\hat{L}$ increases), the fibre becomes more aligned and streamlined with the main flow: thus the drag should decrease gradually in this case (notice that Re is constant). However our simulation result suggests the opposite which may be explained as follows: as $\hat{L}$ increases, the boundary layers on the channel entry portion (above the tethered point of the fibre) on the two sidewalls have almost the same thickness (see figure 9). Therefore the fraction of the boundary layers' thickness with respect to the channel width increases, and the fraction of the channel width available to the freely flowing fluid (outside the boundary layers) decreases. Because the inlet flow speed is the same, the oncoming flow towards the fibre possesses a greater 'effective speed' than the inlet speed. Hence the fibre experiences more drag as $\hat{L}$ increases. This effect seems to reach a maximum when $\hat{L}$ reaches approximately 0.6. After that the C_d–$\hat{L}$ curve levels off. This also explains why the fibre gets more aligned with the mainstream flow as $\hat{L}$ increases, as shown in the bottom panels of figure 9.

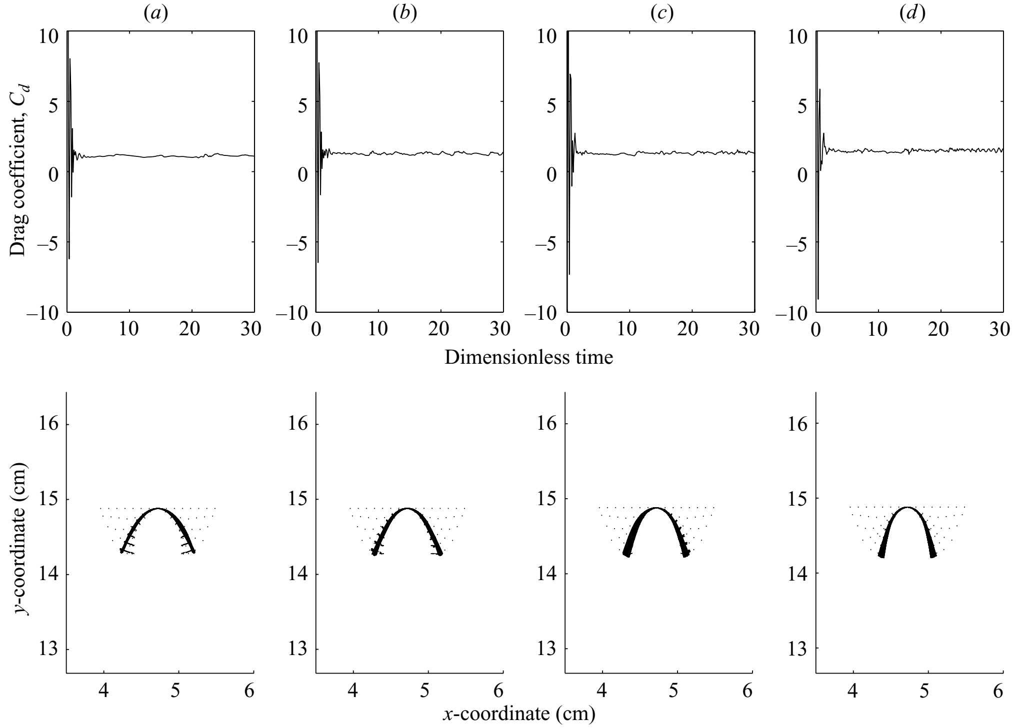

FIGURE 10. The drag coefficient and position of the fibre at four different values of fibre length. The upper panels plot the drag as a function of time and the lower panels plot the corresponding position of the fibre. The dotted and solid lines are the fibre positions before and after it reaches the 'quasi-steady' state, respectively. The thickness of the solid lines (many lines overlap) represents the fibre oscillation range. The value of $\hat{L}$ is (*a*) 0.1778, (*b*) 0.4, (*c*) 0.6, (*d*) 0.8.

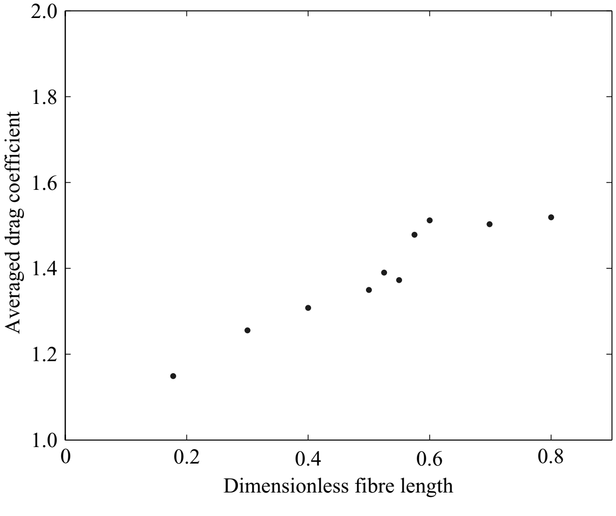

FIGURE 11. The averaged drag coefficient $\bar{C_d}$ versus dimensionless fibre length $\hat{L}$.

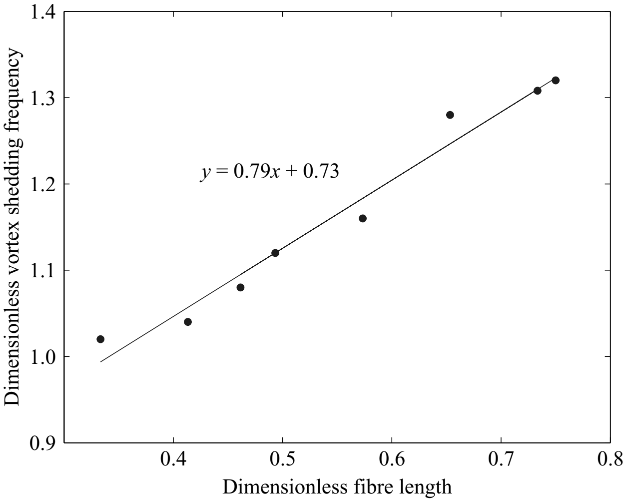

FIGURE 12. Dimensionless vortex shedding frequency f_{vs} versus dimensionless fibre length $\hat{L}$. The data show that f_{vs} increases as $\hat{L}$ increases. The line fitting the data best in the least squares sense is $y = 0.79x + 0.73$.

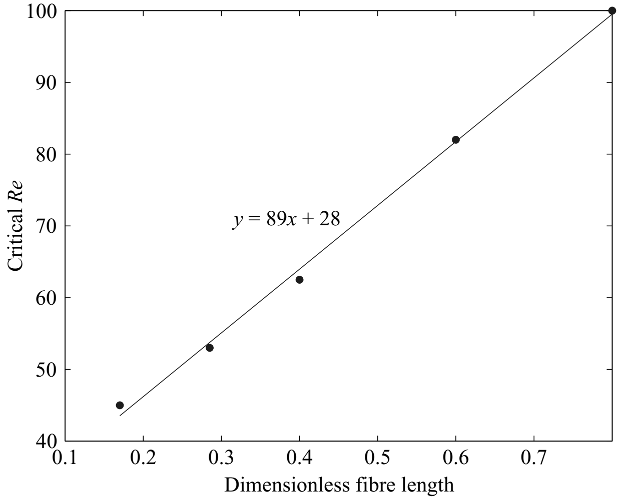

FIGURE 13. Critical Reynolds number Re_c versus dimensionless fibre length $\hat{L}$. The Re_c increases as $\hat{L}$ increases. The best-fitting line by the least squares is $y = 89x + 28$.

Figure 12 plots the dimensionless vortex shedding frequency f_{vs} versus dimensionless fibre length $\hat{L}$. f_{vs} increases with $\hat{L}$ in (0.18, 0.75). As already mentioned above, as $\hat{L}$ increases, the effective $\hat{K}_b$ decreases because of the greater effective incoming flow speed. Therefore f_{vs} increases with $\hat{L}$. The line $f_{vs} = 0.79\hat{L} + 0.73$ fits the data best in the sense of the least squares, which indicates that the dimensionless vortex shedding frequency increases approximately linearly with the dimensionless fibre length.

Figure 13 plots the critical Reynolds number Re_c versus dimensionless fibre length $\hat{L}$. It is seen that Re_c increases with $\hat{L}$ in (0.18, 0.75). The line fitting the data by the least squares is $Re_c = 89\hat{L} + 28$. The data for Re_c has an error of ±5. A greater $\hat{L}$ means a narrower flow channel, which imposes a stricter constraint on the wake behind the fibre through its two rigid sidewalls. Therefore it becomes more difficult for the wake to oscillate. This may explain why Re_c is a increasing function of $\hat{L}$.

Basing on the group of simulations with varying dimensionless fibre length, we conclude that the fibre length $\hat{L}$ has a significant influence on the vortex shedding and drag coefficient. Re_c and f_{vs} both increase nearly linearly with the increase of $\hat{L}$. The averaged drag coefficient $\bar{C}_d$ increases with $\hat{L}$ at first and then becomes roughly constant.

4. Summary and discussion

Three sets of simulations have been designed and performed to investigate the influences of the Reynolds number, fibre dimensionless flexure modulus and dimensionless length on the vortex shedding and drag coefficient of the fibre. Our simulations have demonstrated the discernible differences in shed vortices and the consequential fibre vibration and oscillation in drag coefficient. From these simulations, we draw the following conclusions, within the ranges of parameters used in our simulations. (i) The Reynolds number has a significant influence on vortex shedding and fibre vibration. However, the Reynolds number has little influence on the averaged drag coefficient $\bar{C}_d$ for Re in [200, 800]. It appears that the C_d–t curve becomes somewhat less oscillatory as Re increases. (ii) The fibre dimensionless flexure modulus has a significant influence on vortex shedding, fibre vibration and the C_d–t curve. As $\hat{K}_b$ increases, both the dimensionless vortex shedding frequency f_{vs} and the critical Reynolds number Re_c decrease, approximately in the form of power laws. (iii) The dimensionless fibre length has a significant influence on vortex shedding, fibre vibration and the C_d–t curve. Re_c and f_{vs} each increases linearly with $\hat{L}$. $\bar{C}_d$ increases with $\hat{L}$ at first and then becomes insensitive to $\hat{L}$.

Williamson & Govardhan (2004) classified vortex shedding from an elastically mounted cylinder into three major patterns: the 2S mode (two single vortices per cycle), the 2P mode (two vortex pairs per cycle) and the P + S mode (a vortex pair and a single vortex per cycle). Our simulations show that vortex shedding from a flexible fibre with the mid-point tethered belongs to the 2S mode. Neither a 2P mode nor a P + S mode was found. Compared to the vortex shedding seen in the figure 2 of Alben *et al.* (2004), vortex shedding from our simulations appears different, especially in the wake away from the fibre. Perhaps this is because of the significant difference in Re, which has an important influence on vortex shedding, as illustrated in figure 2 of this paper. The vortex shedding reported here is similar to those observed from a flapping filament in Zhu (2001) and Zhu & Peskin (2002), from two in-phase-flapping filaments in Zhu & Peskin (2003), and from a stationary rubber loop in Jung *et al.* (2006). But it is different from the vortex shedding from two anti-phase-flapping filaments in Zhu & Peskin (2003) (none of the above modes), from the flapping rubber loop in Jung *et al.* (2006) (2P mode), and from the side-by-side cylinders in Wang *et al.* (2005) (very complicated).

According to our simulations, it appears that the degree of oscillation in the C_d–t curve lessens somewhat as Re increases while the fibre vibration range widens. In the laboratory experiment by Alben *et al.* (Re between 2000 and 40 000), no oscillation in the drag or drag coefficient was found. Does the oscillation in drag coefficient completely disappear when Re becomes sufficiently high? This seems to be possible based on our simulations at lower Re. The current Navier–Stokes solver used in the IB method is not accurate for very high-Re flows. At this point we cannot confirm this conjecture, but it seems to be counter-intuitive and may deserve further research.

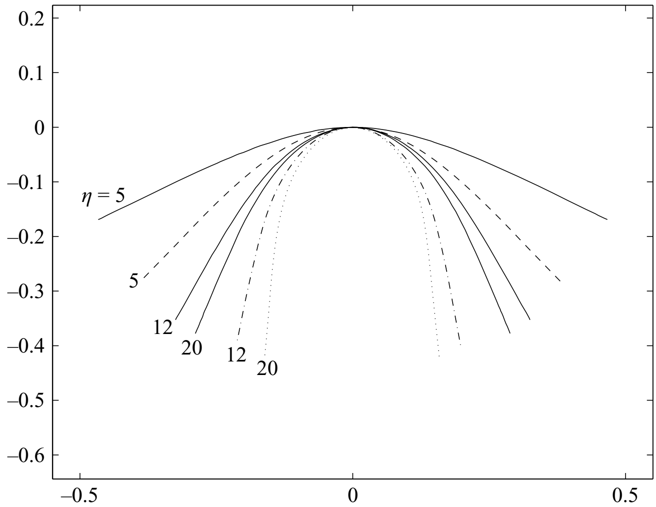

FIGURE 14. Comparison of averaged fibre shapes from our simulations with those in the work of Alben *et al.* (2002). The x and y coordinates are non-dimensionalized by the fibre length (1.95 cm). The three solid lines are results from Alben *et al.* (2002). The values of η for the solid lines are 5, 12, 20 from top to bottom, respectively. Note that the experimental results and numerical results in Alben *et al.* (2002) are almost not distinguishable for the three values of η and only the numerical results are shown here. The other three lines are our simulation results. The value for η is 5 for the dashed line, 12 for the dash-dotted line, and 20 for the dotted line. The relation between η and $\hat{K}_b$ is $\hat{K}_b = 1/2\eta^2$. The Reynolds number for the three simulations is 600 which is approximately 100 times less than the experimental value. This may explain the quantitative differences shown in the figure. Notice that each curve from Alben *et al.* lies above the corresponding curve from our simulation. See the bottom panels of Figure 2 for the influence of Re on fibre shape.

According to our simulations at lower Re, the fibre–fluid problem becomes unsteady when vortex shedding occurs, and the fibre vibration range increases with Re. In Alben *et al.* (2002, 2004) where Re was significantly higher, the flow was steady and the fibre assumes a definite shape and position for a given set of flow parameters. The averaged shape and position of the fibre at the ‘quasi-steady’ state in our simulation are compared in figure 14 with those (both experimental and numerical) reported in figure 3(a) of Alben *et al.* (2002) for three cases ($\eta = 6$, 15, 20)† where the experimental and numerical results in Alben *et al.* (2002) agreed extremely well. It is seen that although the fibre shapes in our simulations were similar to those in Alben *et al.* (2002) obvious quantitative differences exist. Notice that the results in Alben *et al.* (2002) are all above our averaged simulation results. The discrepancy between our results and Alben *et al.*’s may be explained by the fact that Re in our simulations is lower by two orders of magnitude. (It appears that the higher Re, the wider the opening of the fibre. See figure 3.) For more comparisons with Alben *et al.*’s work (e.g. drag), see Zhu & Peskin (2007).

Presumably the oscillation in the C_d–t curve is caused by the vibration of the fibre which is induced by vortex shedding. It is expected that there exist functional relationships among the frequencies of oscillation in C_d, in fibre vibration and vortex

---

† η is defined as $\sqrt{\frac{1}{2}\rho_0 L^3 V_0^2/K_b}$ in Alben *et al.* (2002). It measures the relative importance of fluid kinetic energy and elastic potential energy. The relationship between η and $\hat{K}_b$ is $\hat{K}_b = 1/(2\eta^2)$.

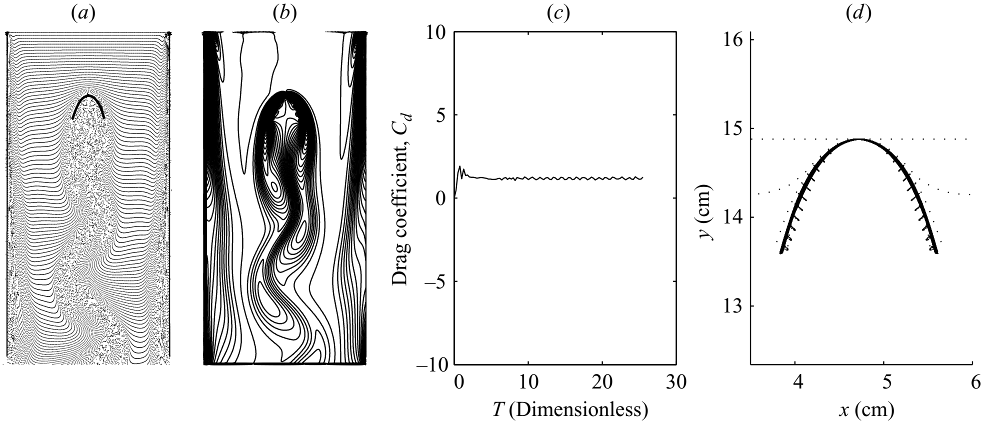

FIGURE 15. The simulation results where the FFT analysis on C_d–t data reveals a single distinct frequency. The parameters used for this simulation were $L = 3.3$ cm, $K_b = 2.8$ erg cm, $\nu = 4\,\text{cm}^2\,\text{s}^{-1}$, $V_0 = 212.5\,\text{cm}\,\text{s}^{-1}$. (The dimensionless parameters are: $Re = 175$, $\hat{K}_b = 0.0065$, $\hat{L} = 0.3667$, $Fr = 14$, $\hat{K}_s = 5.369 \times 10^6$.) (*a*) The positions of fluid markers. (*b*) The vorticity contours. (*c*) The drag coefficient versus time. (*d*) The positions of the fibre. The oscillation in C_d–t has a distinct frequency of 125 Hz. The vortex shedding frequency is 75 Hz.

shedding. However, the fibre vibration is more complicated than expected. Unlike the 'simple' periodic up-and-down flapping with a single frequency of a flexible rod supported at the middle point, the flexible fibre vibrates in a more complicated fashion in the flowing fluid. Although not shown here, from an animation based on the simulation, it is seen that small-amplitude 'irregular' vibrations occur almost everywhere on the fibre except near the tethered point. According to our simulations the vibration induced by vortex shedding is always small (in terms of amplitude compared to its length) and the lock-in phenomenon described in Williamson & Govardhan (2004) was not found. It seems that the small-amplitude vortex-shedding-induced vibration is 'lost' in the background 'noise' (the localized irregular motions). This makes the fibre motion difficulty to quantify: only the range of the fibre position is given here. Fibre flexibility and interaction with the local fluid flowing past are supposed to be responsible for the complexity of fibre motion. Consequentially, FFT analysis performed on the C_d–t data revealed distinct frequencies only in a few cases. (It is not yet clear what is the underlying reason for this.) However, no quantitative relationship between the frequency and vortex shedding frequency was found for these cases. One such example is given below. Figure 15 shows the results for a simulation with a 3.3 cm fibre with bending modulus 2.8 erg cm in a flowing fluid with kinematic viscosity 4 $\text{cm}^2\,\text{s}^{-1}$. The inflow speed was 212.5 cms^{-1}. (The dimensionless parameters are: $Re = 175$, $\hat{K}_b = 0.0065$, $\hat{L} = 0.3667$, $Fr = 14$, $\hat{K}_s = 5.369 \times 10^6$.) Figure 15(*a*) plots the positions of fluid markers at $T = 26$. Figure 15(*b*) plots the vorticity contours at the same instant. Figure 15(*c*) plots the C_d–t curve. Figure 15(*d*) plots the fibre shape and position with time. See the caption for details. Application of FFT on the C_d–t data reveals a single distinct frequency, approximately 125, which is supposed to be the oscillation frequency in C_d. The vortex shedding frequency for this case was found to be 75.

The author would like to thank the unknown Referees for their suggestions and comments which have helped him for a better representation of his work. The author also thanks Silas Alben and Jun Zhang for providing their numerical and experimental data.

REFERENCES

ABARBANEL, S. S., DON, W. S., GOTTLIEB, D., RUDY, D. H. & TOWNSEND, J. C. 1991 Secondary frequencies in the wake of a circular cylinder with vortex shedding. *J. Fluid Mech.* **225**, 557.

ALBEN, S. 2004 Drag reduction by self-similar bending and a transition to forward flight by a symmetry breaking instability. PhD thesis, Courant Institute of Mathematical Sciences, New York University.

ALBEN, S., SHELLEY, M. & ZHANG, J. 2002 Drag reduction through self-similar bending of a flexible body. *Nature* **420**, 479.

ALBEN, S., SHELLEY, M. & ZHANG, J. 2004 How flexibility induces streamlining in two-dimensional flow. *Phys. Fluids* **16**, 1694.

BEARMAN, P. W. 1989 Vortex shedding from oscillating bluff bodies. *Annu. Rev. Fluid Mech.* **16**, 195.

GRIFFIN, O. M. & RAMBERG, S. E. 1982 Some recent studies of vortex shedding with application to marine tubulars and risers. *Trans. ASME: J. Energy Resour. Technol.* **104**, 2.

JUNG, S. W., MARECK, K., SHELLEY, M. & ZHANG, J. 2006 Dynamics of a deformable body in a fast flowing soap film. *Phy. Rev. Lett.* **97**, 134502.

KRASNY, R. 1990 Vortex sheet roll-up due to the motion of a flat plate. In *International Symposium on Nonsteady Fluid Dynamics* (ed. J. A. Miller & D. P. Telionis). ASME FED Vol. 92.

LEE, S. 2000 A numerical study of the unsteady wake behind a sphere in a uniform flow at moderate Reynolds numbers. *Computers & Fluids* **29**, 639.

NITSCHE, M. & KRASNY, R. 1994 A numerical study of vortex ring formation at the edge of a circular tube, *J. Fluid Mech.* **276**, 139.

PARKINSON, G. V. 1989 Phenomena and modelling of flow-induced vibrations of bluff bodies. *Prog. Aerosp. Sci.* **26**, 169.

PESKIN, C. S. 1977 Flow patterns around heart valves: a numerical method. *J. Comput. Phys.* **25**, 220.

PESKIN, C. S. 2002 The immersed boundary method. *Acta Numerica* **11**, 479.

PESKIN, C. S. & MCQUEEN, D. M. 1996 Fluid dynamics of the heart and its valves. In *Case Studies in Mathematical Modeling: Ecology, Physiology, and Cell Biology* (ed. H. G. Othmer, F. R. Adler, M. A. Lewis & J. C. Dallon), p. 309. Prentice-Hall.

SARPKAYA, T. 1975 An inviscid model of two-dimensional vortex shedding for transient and asymptotically steady separated flow over an inclined flat plate. *J. Fluid Mech.* **68**, 109.

SARPKAYA, T. 1979 Vortex-induced oscillations. *Trans. ASME: J. Appl. Mech.* **46**, 241.

WANG, Z. J. & ZHOU, Y. 2005 Vortex interactions in a two side-by-side cylinder near-wake. *Intl J. Heat Fluid Flow* **26**, 362.

WILLIAMSON, C. H. K. & GOVARDHAN, R. 2004 Vortex-induced vibrations. *Annu. Rev. Fluid Mech.* **36**, 413.

ZHU, L. 2001 Simulation of a flapping flexible filament in a flowing soap film by the immersed boundary method. PhD thesis, Courant Institute of Mathematical Sciences, New York University.

ZHU, L. & PESKIN, C. S. 2002 Simulation of a flapping flexible filament in a flowing soap film by the immersed boundary method. *J. Comput. Phys.* **179**, 452.

ZHU, L. & PESKIN, C. S. 2003 Interaction of two flapping filaments in a flowing soap film. *Phys. Fluids* **15**, 1954–1960.

ZHU, L. & PESKIN, C. S. 2007 Drag of a flexible fibre in a two-dimensional moving viscous fluid. *Computers & Fluids*, **36**, 398.